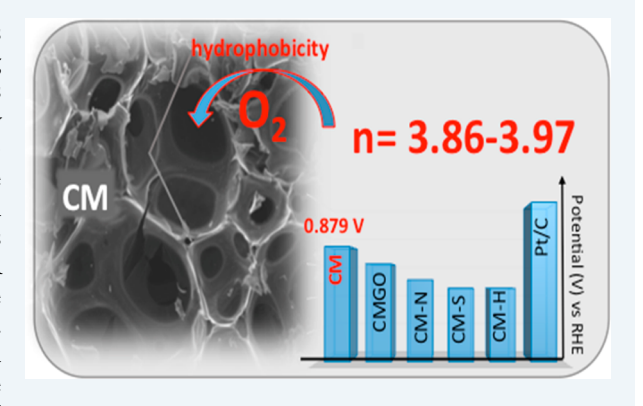


Combined Effect of Porosity and Surface Chemistry on the Electrochemical Reduction of Oxygen on Cellular Vitreous Carbon Foam Catalyst

Jimmy Encalada,[†] Keerthi Savaram,[‡] Nikolina A. Travlou,[§] WanLu Li,[§] Qingdong Li,[‡] Clara Delgado-Sánchez, Vanessa Fierro, Alain Celzard, Huixin He, and Teresa J. Bandosz**, So

Supporting Information

ABSTRACT: A new mechanism of O2 reduction, which follows principles different from those generally accepted for describing ORR reduction on heteroatom-doped carbons, is suggested. It is based on the ability of oxygen to strongly adsorb in narrow hydrophobic pores. In this respect, a cellular vitreous carbon foamgraphene oxide composite was synthesized. The materials were doped with sulfur and nitrogen and/or heat-treated at 950 °C in order to modify their surface chemistry. The resultant samples presented a macro-/microporous nature and were tested as ORR catalysts. To understand the reduction process, their surfaces were extensively characterized from texture and chemistry points of view. The treatment applied markedly changed the volumes of small micropores and the surface hydrophilicity/polarity character. The results showed that the electron transfer number was between 3.87



and 3.96 and the onset potential reached 0.879 V for the best-performing sample. It is noteworthy that the best-performing sample has the highest volume of pores smaller than 0.7 nm while there was no heteroatom doping. The hydrophobicity and the strong adsorption forces provided by these pores to pull oxygen inside are the possible reasons for the observed excellent performance. A decrease in the volume of these pores resulted in a decrease in the catalytic performance. When the surface was modified with heteroatoms, the performances worsened further because of the induced hydrophilicity.

KEYWORDS: O2 reduction, carbon, electrocatalysis, porosity, surface chemistry, specific interactions

1. INTRODUCTION

The oxygen reduction reaction, ORR, is of significant importance for the development of new sources of energy.^{1,2} So far, platinum carbon cathodes are considered as the best catalysts for this process. Nevertheless, they exhibit certain drawbacks, including the high cost of Pt, a low tolerance to fuel/methanol crossover, and poor operation durability. All of these have directed the attention of researchers to the development of non-noble-metal or nonmetal electrocatalysts, which could have a sufficient performance in the ORR and could be used as replacements for Pt/C materials.3-16 Nonmetal electrocatalysts are mainly based on heteroatom-doped carbons. ^{13–15,17–25} So far, research efforts have focused on nonporous carbonaceous catalysts such as graphene oxide and graphene.^{3,4,6–9,11,16} To increase the efficiency of the process, nitrogen, ^{5,6,8,10,13,14,23} sulfur, ^{7,9,11,15,24,25} phosphorus, ^{18,21,22} and boron, ^{21,26} either alone or codoped, ^{15,17} have

been introduced into the carbon matrix. They have been indicated as providing catalytic active sites for oxygen electrosorption and reduction. 3,9,11,17,26

Doping with nitrogen has been identified as providing the highest number of electron transfer (n), high density of kinetic currents (J_k) , and/or low onset potentials. ^{13,27} On N-doped carbons, n close to 4e⁻ and kinetic current reaching 4 mA cm⁻² $(n = 3.96e^{-} \text{ and } J_k = 4.02 \text{ mA cm}^{-2} \text{ at } -0.50 \text{ V vs SCE } (0.51 \text{ V})$ vs RHE)) have been reported.²⁷ Interestingly, on polyanilinederived N- and O-doped mesoporous carbons, the shift in the onset potential to more positive value with respect to Pt was found with a kinetic current density reaching ~29 mA cm⁻² even though the reported n value was only $2.7e^{-.13}$ This good

Received: June 17, 2017 Revised: September 15, 2017 Published: September 20, 2017



[†]Department of Chemistry, The City College of New York, 160 Convent Avenue, New York, New York 10031, United States [‡]Department of Chemistry, Rutgers University, 73 Warren Street, Newark, New Jersey 07102, United States

[§]Ph.D. Program in Chemistry, The Graduate Center of the City University of New York, New York, New York 10016, United States Ilnstitut Jean Lamour, UMR Université de Lorraine-CNRS No. 7198, ENSTIB, 27 rue Philippe Séguin, BP 21042, 88051 Epinal cedex 9, France

performance was attributed to nitrogen groups in a pyridinic configuration.

Another heteroatom used to dope carbons in order to improve their catalytic performance is sulfur. ^{24,25} In addition to providing catalytic centers for oxygen reduction, sulfur species might also attract oxygen. Reduced sulfur groups (in bisulfides and thiophenic configurations), when they are located in very small pores, were found to help to withdraw oxygen from water/electrolyte. ^{24,25,28,29} These oxygen molecules are then strongly adsorbed in the pores whose width is similar to the size of O₂ molecules. This probably happens due to their surface hydrophobicity and overlapped adsorption potential. Other sulfur species, such as sulfoxide and sulfones, on the other hand, can promote a transport of aqueous electrolyte (with dissolved oxygen) to the small pores where oxygen reduction is enhanced. Their hydrophilicity and their probable existence in larger pores only are crucial assets for this process.

Even though doping solely with nitrogen or sulfur can certainly improve the performances of carbon, codoping with both heteroatoms was reported to bring even better results. On S- and N-codoped graphitic microporous carbon nanospheres, $n=3.8e^-$ and $J_k=27.0$ mA cm⁻² at -0.70 V vs Ag/AgCl (0.28 V vs RHE) were recorded. On mesoporous codoped graphene (S and N), $n=3.3e^-$ and $J_k=24.5$ mA cm⁻² at -0.50 V vs Ag/AgCl (0.48 V vs RHE) were associated with the synergy of charge and spin densities. In the majority of those studies on applications of carbons as ORR catalysts, their performances have been reported as lower than those of Pt/C in terms of the desired $4e^-$ electron pathway and onset potential for fuel cell applications. Nevertheless, in contrast to Pt/C, they show a high tolerance to methanol crossover. 9,11,27

There are not many studies on applications of highly porous carbon materials as ORR reduction catalysts. 13,24,25 These specific materials were even not mentioned in the recent review by Dai and co-workers. 31,32 It is well-known that a high porosity is beneficial for the dispersion/distribution of heteroatoms on the surface, and most studies so far have focused on this aspect. 24,25,28,29 Sung and co-workers 33 studied the role of predefined porosity in ORR catalytic site formation in Fe- and N-codoped carbons. Even though the catalytic activity was mainly linked to Fe-N-C sites in the carbon matrix, the developed porosity promoted enhanced ORR activity by contributing to the high dispersion of active sites. Porous carbon was investigated as a support for Au nanoparticles, and the obtained results of ORR activity were comparable to those on commercial 20% Pt/C.³⁴ The porosity in a carbon material also improved the distribution of Pt catalytic centers on the surface and thus increased their efficiency with respect to the ORR.³⁵ The effects of porosity on the oxygen reduction on Ptfree carbon-based catalysts containing nitrogen, iron, and zinc was investigated by Yin and co-workers.³⁶ They found that optimized porosity facilitated mass transport and thus enhanced fuel cell performances.

Recently, it has been indicated that porosity is not only important for dispersing active metal-containing centers but also promotes in a very specific way the high ORR catalytic activity of hydrophobic microporous metal-free carbon materials.³⁷ On these carbons at a potential of 0.18 V vs RHE, *n* reached 4 with a kinetic current of 35 mA cm⁻², and an onset potential of 0.822 V vs RHE was recorded. Interestingly, these materials had only traces of nitrogen and less than 10 atom % of oxygen, mainly in epoxy groups. Moreover, a dependence of the kinetic current on the volume of pores

smaller than 0.7 nm, where oxygen can be strongly adsorbed, was found.

An interesting approach explaining the activity of pure carbon nanocages was proposed by Hu and co-workers.³⁸ Combining experiments with theoretical calculations, they found that intrinsic carbon defects, born in the carbon matrix, contribute to the observed enhanced ORR activity, irrespective of the presence of nitrogen. They suggested that zigzag edge defects or pentagon defects provide the catalytic activity for ORR, and the number of these defects might be increased in heteroatom-doped carbons. In their most active carbon, not only pores with sizes of less than 1 nm were present but also a high volume of pores with sizes of about 10 nm was detected. High surface area was linked to the existence of intrinsic defects and thus to the high ORR activity. Nevertheless, the electron transfer number was only 2.9. The role of carbon catalyst geometry in the ORR was also investigated by Dai and coworkers.³⁹ Although they addressed N- and Fe-doped CNT/ graphene complexes, their research suggested that unzipped walls of nanotubes provided the catalytic activity and that the charge transport was facilitated due to the intact electrical conductivity of the CNT/graphene. Those unzipped fragments, referred to by the authors as graphite oxide pieces, provided abundant edges and defect sites enhancing ORR catalytic activity.

To challenge the general belief that doping with nitrogen or sulfur makes the surface of carbon most active for ORR and to further evaluate the combined role of porosity for this process, cellular vitreous carbon foams of high volumes of micropores and macropores, as such and chemically modified, were evaluated as ORR catalysts. They were obtained by frothing aqueous solutions of biosourced phenolic resins, followed by polymerization of the resultant liquid foams and subsequent pyrolysis at 900 °C. 40 The presence of large pores made it possible to impregnate these foams with graphene oxide (GO) in order to modify both porosity and surface chemistry. To further alter surface chemistry, S and N heteroatoms were introduced. An advance in comparison to the state of the art in the field demonstrates that the ORR is enhanced by adsorption processes and that hydrophobic pores of small sizes are crucial features of the catalysts. Having this in mind, we also provide further insight into the way heteroatoms and their specific forms existing inside the pore structure affect the ORR process. The materials were extensively characterized to link their catalytic behavior to the target surface features.

2. EXPERIMENTAL SECTION

2.1. Materials. Cellular vitreous carbon foam was prepared as described in refs 40 and 41. Briefly, a 40 wt % aqueous solution of tannin extract, a plant-derived polyphenol, was prepared to which a cross-linker (hexamine), a polymerization catalyst (pTSA), and a surfactant (Cremophor ELP) were added. The resultant brown homogeneous solution was vigorously stirred with a blade mixer until a thick, viscous, and stable liquid foam was obtained. The latter was hardened in an oven at 85 °C for 24 h and then dried at room temperature for a few additional days. Finally, the rigid thermoset foam that was recovered was pyrolyzed at 900 °C in a flow of very pure nitrogen, leading to a cellular monolith made of vitreous carbon. Due to the similarity of such a process with the recipe for meringues, according to which egg whites are whipped until stiff and then hardened in an oven, this special kind of carbon

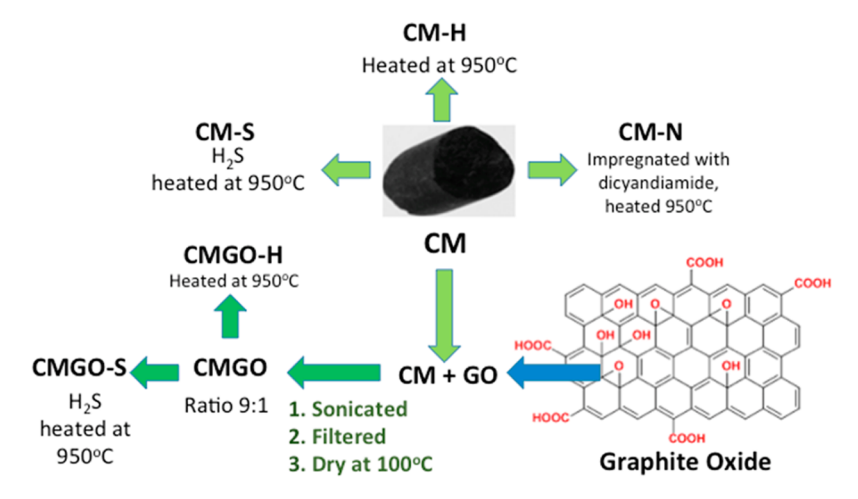


Figure 1. Schematic view of the samples' modification procedure.

foam is called "carbon meringue" ⁴¹ and referred to as CM in the following discussion.

Graphite oxide (GO) was prepared using the Hummers method. ⁴² A 0.555 g portion of GO was sonicated for 1 h and combined with 4.00 g of CM. The mixture was further sonicated for another 1 h. Then the sample was filtered and dried at 120 °C. The composite is referred to as CMGO. It contains 90% CM and 10% GO.

In order to introduce nitrogen into CM, the sample was mixed with dicyandiamide at a ratio of 1:1. Then the mixture was heated in a horizontal furnace at 950 $^{\circ}$ C at a heating rate of 10 $^{\circ}$ C min⁻¹ in a flow (100 mL min⁻¹) of nitrogen for 1 h. The modified sample is referred to as CMN.

To prepare the carbon composites with sulfur, 2 g of CM or CMGO was placed in a horizontal furnace and exposed to 1000 ppm of $\rm H_2S$ in nitrogen at a flow rate of 100 mL min⁻¹. The heating rate was 10 °C min⁻¹, the final temperature 950 °C, and the dwell time 1 h. The samples after that treatment are referred to as CM-S or CMGO-S, respectively. We arbitrarily decided to investigate to a greater extent the effect of oxygen in the carbon matrix on the surface chemistry and thus on the catalytic behavior of sulfur-doped materials. The effect of nitrogen on the catalytic behavior of ORR carbon-based catalyst is well described in the literature, and only modification of the initial sample, CM, toward introduction of some N-containing groups was carried out.

CM and CMGO were also heat-treated for 1 h at 950 $^{\circ}$ C, with a heating rate of 10 $^{\circ}$ C min⁻¹ under 100 mL min⁻¹ of nitrogen. The corresponding samples are referred to as CM-H and CMGO-H, respectively.

The preparation steps are illustrated in Figure 1. For reference, Pt/Vulcan catalytic carbon with 20 wt % platinum (Sigma-Aldrich) was used.

2.2. Methods. 2.2.1. Electrochemical Measurements. The CV (cyclic voltammetry) and LSV (linear sweep voltammetry) of the as-prepared samples were analyzed by using a computer-controlled potentiostat (CHI 760C, CH Instruments, USA). A typical three-electrode cell was used with platinum wire as the counter electrode, Ag/AgCl (1 M KCl) as the reference electrode, and a rotating ring-disk electrode (RRDE) as the working electrode in 0.1 M KOH for the electrochemical measurements. The working electrodes were prepared by dispersing 5 mg of the as-prepared catalyst in 1 mL of deionized water and 0.5 mL of 1 wt % Nafion aqueous solution by

sonication and drop-casting 15 μ L of the above dispersed solution onto the RRDE. The dried electrode was immersed into the 0.1 M KOH solution, which was saturated with N2 gas for 1 h, and the CV curves were recorded 10 times at a scan rate of 100 mV s^{-1} for stabilization of the catalysts. The potential was swept from 0.19 to -0.8 V vs Ag/AgCl (1.17 to 0.18 V vs RHE). The CV curves were overlaid one over another to check if the electrode was stabilized, and then two CV curves were recorded at a scan rate of 5 mV s⁻¹ in the N₂-saturated 0.1 M KOH electrolyte. Next, the electrolyte was saturated with O₂ for 30 min and two CV curves were recorded at a scan rate of 5 mV s⁻¹. This step was repeated one more time and overlaid to determine that there was no change in the onset and peak potentials. Finally, LSV measurements were carried out at different rotation speeds (400–2000 rpm) with continuous O₂ purging. The percent peroxide generated (eq 1) and the electron transfer number (eq 2) were calculated from the LSV curves using the equations

$$\% \text{ HO}_2^- = \frac{200\frac{I_r}{N}}{I_d \frac{I_r}{N}} \tag{1}$$

$$n = \frac{4I_{\rm d}}{I_{\rm d} + \frac{I_{\rm r}}{N}} \tag{2}$$

where $I_{\rm d}$ and $I_{\rm r}$ are the ring and disk currents measured with RRDE. All experiments were conducted at room temperature, and the collection efficiency number N was determined to be 0.424 from the redox reaction of $K_3 Fe(CN)_6$. The onset potential was chosen as the highest potential for the cathodic reactions at which a reaction product is formed at a given electrode. The corrections for capacitive current were applied in all data analyses.

To study the tolerance of the carbon catalysts to methanol, 0.2 mL of $\rm CH_3OH$ was placed in the electrochemical cell. The final concentration of methanol (0.2 mL, three times) added to the electrochemical cell (40 mL, 0.10 M KOH) was 0.36 M. The working electrode was prepared by mixing the active material with polyvinylidene fluoride (PVDF) and commercial carbon black (acetylene black, 50% compressed, Alfa Aesar) (8:1:1) in N-methyl-2-pyrrolidone.

The stability tests were done by running 1000 CV cycles in the potential range of -0.1 to -0.5 V vs Ag/AgCl (0.88 to 0.48 V vs RHE) in an O_2 -saturated electrolyte after the stabilization

of the electrode in a nitrogen-saturated electrolyte in the potential range of 0.19 to -0.8 V vs Ag/AgCl (1.17 to 0.18 V vs RHE). The currents at the maximum of the ORR reduction hump were used to evaluate the catalyst stability.

The measured potentials versus the Ag/AgCl (1 M KCl) reference electrode were converted to the reversible hydrogen electrode (RHE) scale using the Nernst equation:⁴³

$$E_{\text{RHE}} = E_{\text{Ag/AgCl}} + 0.059 \text{pH} + E^{\circ}_{\text{Ag/AgCl}}$$
(3)

where $E_{\rm RHE}$ is the converted potential versus RHE, $E_{\rm Ag/AgCl}$ is the experimental potential measured against the Ag/AgCl reference electrode, and $E^{\circ}_{\rm Ag/AgCl}$ is the standard potential of Ag/AgCl (1 M KCl) at 25 °C (0.235 V). The electrochemical measurements were carried out in 0.10 M KOH (pH 13) at room temperature; therefore, $E_{\rm RHE} = E_{\rm Ag/AgCl} + 1.002$ V.

The geometric surface area of the rotating ring-disk electrode is 0.126 cm^2 , as determined from geometrical measurements. Since the nanopores of the catalysts are accessible for oxygen molecules but possibly not for larger molecules such as $K_3Fe(CN)_6$, the effective surface areas cannot be accurately measured by the generally used chronocoulometry of $K_3Fe(CN)_6$ method. Thus, the effective surface areas reported here are directly calculated from the weight of the catalyst loaded on the electrode and its BET surface area measured from adsorption of nitrogen. They are 320.0, 298.0, 314.0, 327.5, 196.5, 251.5, and 242.5 cm² for CM, CMGO, CM-H, CMGO-H, CM-N, CM-S, and CMGO-S, respectively.

2.2.2. Scanning Electron Microscopy (SEM). Scanning electron microscopy (SEM) images were obtained with a FEI Helios NanoLab 48 instrument. The accelerating voltage was 5.00 kV. The imaging was performed in situ on the powder samples, using a gold layer 5 nm thick.

2.2.3. Mercury Porosimetry. Mercury porosimetry was carried out using an AutoPore IV 9500 device (Micrometrics, USA), according to two steps: (i) evacuation of the sample holder with the material inside and filling with mercury in a low-pressure chamber within the pressure range 0.001–0.24 MPa and (ii) transfer of the sample holder filled with sample and mercury to a high-pressure chamber and pressure increase from 0.24 to 414 MPa. The entrance diameters of pores in which mercury was forced to penetrate were estimated by application of Washburn's equation:

$$D = -\frac{4\gamma \cos \theta}{P} \tag{4}$$

where D (nm) is the intruded pore size, γ (485 mJ m⁻²) is the surface tension of mercury, θ (140°) is the contact angle between the mercury and the material, and P (MPa) is the intrusion pressure.

2.2.4. Evaluation of Porosity. Sorption of nitrogen at -196 °C was carried out using an ASAP 2020 instrument (Micromeritics, Surface Area and Porosity Analyzer). Before the experiments, samples were outgassed at 250 °C to constant vacuum (2 × 10⁻⁶ Torr) for more than 48 h. The temperature and long degassing time were chosen on the basis of the results of thermal analysis indicating that no surface groups decompose at lower temperatures from these carbons. The BET surface area, total pore volumes, $V_{\rm t}$ (from the last point of isotherm at relative pressure equal to 0.99), micropore volume, volume of pores narrower than 0.7 and 1 nm, $V_{\rm <0.7\,nm}$ and $V_{\rm <1\,nm}$, respectively, and mesopore volumes along with pore size distributions were calculated from the isotherms. The volume of mesopores, $V_{\rm meso}$, represents the difference between total

pore and micropore volumes. The volume of pores and pore size distribution were calculated using the 2D-NLDFT approach assuming a heterogeneous surface of pore walls.⁴⁴

2.2.5. Potentiometric Titration. Potentiometric titration (PT) measurements were performed with an 888 Titrando automatic titrator (Metrohm). Details of the experimental procedure are presented in the literature. The experimental data were transformed into proton-binding curves, Q, representing the total amount of protonated sites. From them the pK_a distributions and the numbers of groups represented by certain pK_a values were calculated.

2.2.6. X-ray Photoelectron Spectroscopy (XPS). The XPS measurements were carried out using a Physical Electronics PHI 5000 VersaProbe II spectrometer with a monochromatic Al K α source (1486.6 eV) operating at 15 kV and 50 W, with 10⁻⁸ Pa vacuum in the analyzer chamber. High-resolution spectra of powdered samples were recorded at a takeoff angle of 45° with a constant pass energy value of 29.35 eV, using a 200 μm diameter analysis area, while 117.4 eV pass energy was used for the survey spectra and used for the calculation of surface atomic concentration. The spectrometer energy scale was calibrated using Cu $2p_{3/2}$, Ag $3d_{5/2}$, and Au $4f_{7/2}$ photoelectron lines at 932.7, 368.3, and 84.0 eV, respectively. The SmartSoft-VP2.6.3.4 software package was used for acquisition and data analysis, and the Multipack software was used to fit photoelectron spectra. A Shirley-type background was subtracted from the signals. Recorded spectra were always fitted using Gauss-Lorentz curves in order to determine the binding energy of the different element core levels more accurately.

2.2.7. Thermal Analysis. Thermogravimetric (TG) curves were obtained using a TA Instruments thermal analyzer (SDT Q 600), which was connected to a gas analysis system (OMNI Star) mass spectrometer. The carbon sample was heated to 1000 °C (10 °C min⁻¹) under a constant helium flow (100 mL min⁻¹). From the TG curves, differential TG (DTG) curves were derived.

2.2.8. Water Adsorption. Prior to water adsorption, the CM series of samples were dried at 120 °C for 12 h and then cooled in a desiccator to room temperature. Afterward, the predetermined amounts of dry samples were exposed to water vapors (30 mL of water in a 1.1 L closed vessel) in airtight environments for 24 h at 22 °C. The amounts adsorbed were measured gravimetrically using a TA Instruments thermal analyzer (SDT Q 600). The weight loss in nitrogen between 30 and 120 °C was assumed as being equivalent to the quantity of water adsorbed on the surface.

2.2.9. Metal Content Analysis. The metal content analysis (of the ashes) was done in Asbury Carbons using an ICP atomic adsorption spectrometer (Varian, Vista MPX ICP-OES). The sample was placed in a platinum crucible, introduced into a furnace at a low temperature, and then burnt at 700 °C. Approximately 1 g of lithium tetraborate flux was added to the ash and held at 950 °C until the ash constituents were dissolved in the flux. The resultant materials were next dissolved in a hydrochloric acid solution, which was diluted to 200 mL for analysis by ICP-OES. The instrument was calibrated with each use, using a series of aqueous standards, which were matrix-matched as closely as possible to the unknown samples.

3. RESULTS AND DISCUSSION

3.1. Materials Characterization. A particular porosity in the range of micro- and macropores of the carbon meringues

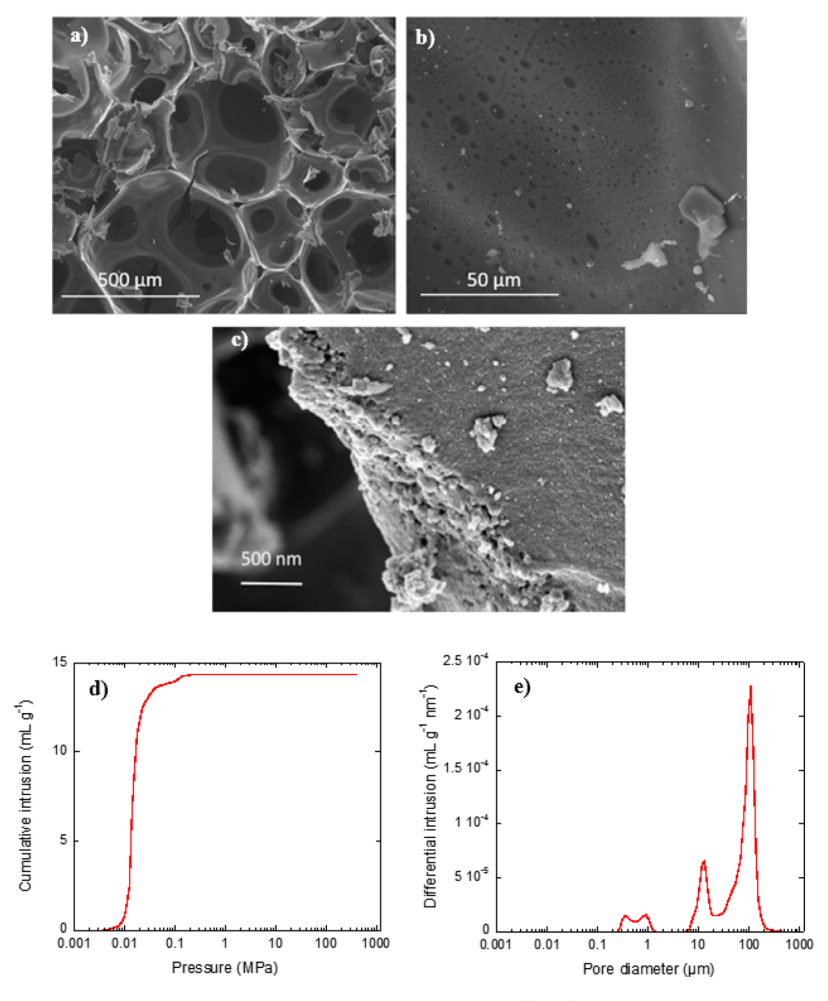


Figure 2. (a-c) SEM images of the CM sample at different magnifications and (d, e) cumulative and differential mercury intrusion curves, respectively.

Table 1. Parameters of Porous Structures Calculated from Nitrogen Adsorption Measurements Using the 2D-NLDFT Model^a and Affinity of Carbons toward Water Vapor

sample	$S_{\rm BET}~({\rm m^2~g^{-1}})$	$V_{\rm t}~({\rm cm}^3~{\rm g}^{-1})$	$V_{\rm meso}~({\rm cm}^3~{\rm g}^{-1})$	$V_{<0.7\mathrm{nm}}~(\mathrm{cm}^3~\mathrm{g}^{-1})$	$V_{<1{\rm nm}}~({\rm cm}^3~{\rm g}^{-1})$	$V_{\mathrm{mic}}~(\mathrm{cm^3~g^{-1}})$	$V_{ m mic}/V_{ m t}$	H_2O^b (wt %)
CM	640	0.324	0.018	0.251	0.279	0.306	0.94	3.65
CMGO	596	0.312	0.031	0.244	0.257	0.281	0.90	5.03
CM-N	393	0.211	0.026	0.135	0.157	0.185	0.88	2.13
CM-S	503	0.285	0.026	0.193	0.223	0.259	0.91	1.64
СМ-Н	628	0.320	0.025	0.234	0.263	0.295	0.92	1.97
CMGO-H	655	0.346	0.036	0.252	0.278	0.310	0.90	2.24
CMGO-S	485	0.287	0.06	0.149	0.193	0.227	0.79	2.26

"Definitions: S_{BET} , BET surface area; V_{ν} total pore volume; V_{meso} , volume of mesopores; $V_{<0.7\,\mathrm{nm}}$ and $V_{<1\,\mathrm{nm}}$, volume of pores narrower than 0.7 and 1 nm, respectively; V_{mic} , micropore volume. "The amount of H_2O adsorbed by GO under the same conditions was 39.8 wt %; GO is nonporous ($S_{\mathrm{BET}} = 6~\mathrm{m}^2~\mathrm{g}^{-1}$).

was a feature that directed us to choose a representative of these groups of porous carbons for further study of ORR efficiency upon various surface modifications. Even though these materials were described in detail in ref 40, Figure 2a–c collects SEM images of CM, whereas Figure 2d,e shows mercury porosimetry data. It can be seen that the material has the typical structure of a carbon foam, with a rather broad distribution of cell sizes roughly ranging from 300 to 600 μ m (see Figure 2a and ref 40 for more details), but with a much narrower distribution of window sizes centered on ca. 100 μ m (see Figure 2a,e). The bulk density of the material was 0.043 g cm⁻³, corresponding to a total porosity of 97.8%. In addition,

the porosity is truly hierarchical, since higher magnification reveals two additional populations of pores having typical diameters of 10 μ m on one hand and below 1 μ m on the other hand (see Figure 2b,e). At the highest magnification, the carbon of which the material is made is based on small nodules, thus resembling the structure of a carbon aerogel (see Figure 2c). Such a feature accounts for the presence of microporosity, as the measured BET surface area was indeed higher than 600 m² g⁻¹ (see below). All of these characteristics were thus expected to favor the deep penetration of the inner porosity by GO flakes. As shown previously, this GO was indeed able to

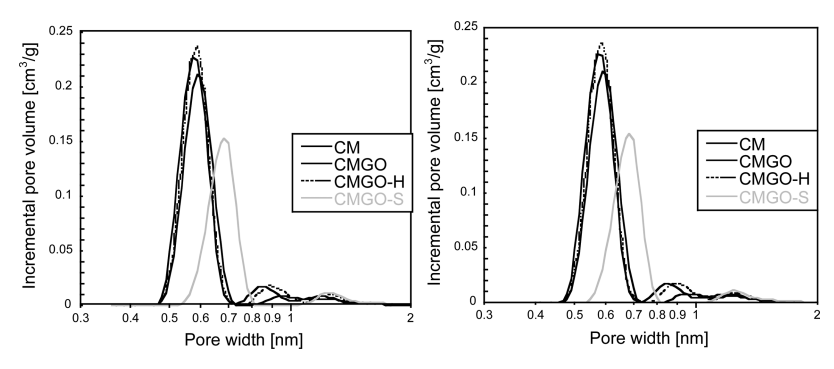


Figure 3. Pore size distributions for the carbons studied, calculated using 2D-NLDFT.

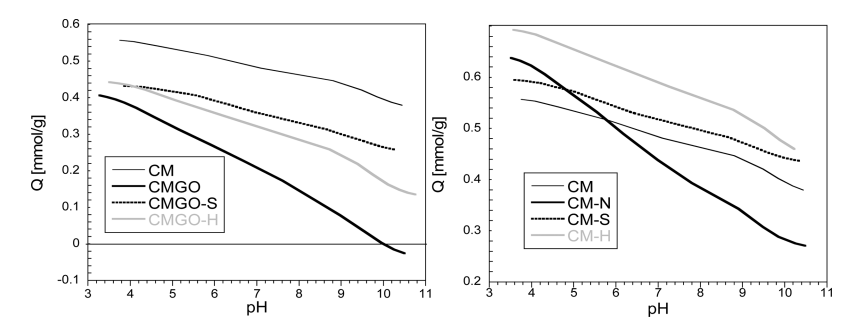


Figure 4. Proton-binding curves.

Table 2. Surface pH Values, Amounts of Groups Detected from Potentiometric Titration (in mmol g⁻¹), and Content of Elements on the Surface Detected by the XPS Analysis (in atom %)

		titration				XP	S	
sample	pН	$pK_a < 7$	$pK_a > 7$	total no. of groups	С	O	N	S
CM	8.83	0.103	0.092	0.195	86.4	13.6	nd ^a	nd
CMGO	7.90	0.243	0.210	0.453	80.7	19.3	nd	nd
СМ-Н	9.07	0.102	0.063	0.165	83.4	14.3	2.3	nd
CMGO-H	8.60	0.115	0.208	0.323	89.6	10.0	3.4	nd
CM-N	8.56	0.197	0.186	0.383	75.6	20.7	3.7	nd
CM-S	9.90	0.102	0.063	0.165	90.7	8.10	nd	<1
CMGO-S	9.29	0.042	0.143	0.185	85.9	14.1	<1	1.2
^a nd = not detected	l.							

penetrate silica gel pores of diameters much smaller than those of carbon meringues.¹¹

Even though macroporosity is important for our modifications, chemical changes in smaller pores that might affect surface interactions with either oxygen or electrolyte are of paramount importance for our research goal. Thus, the nitrogen adsorption isotherms were measured (Figure 1S in the Supporting Information) and the parameters of pore structure and pore size distributions (PSDs) were calculated from them and are presented in Table 1 and Figure 3, respectively. As seen, the addition of 10 wt % GO (GMGO) decreased the surface area, the volume of micropores, and the total pore volume. Interestingly, a marked increase in the volume of mesopores was found. This indicates that GO was deposited in some macropores and its presence indeed decreased their sizes to the range of mesopores. It is important to recall that macropores cannot be detected from nitrogen adsorption studies. Since the shapes of the isotherms for all samples indicate a high degree of microporosity, these pores must exist in the carbon structure/macropore walls, as already suggested by the gel-like appearance seen in Figure 2c. Heating the CMGO composite (CMGO-H) further increased the

volume of micro- and mesopores. These possibly are the results of the reduction of the GO phase. CO, CO2, and water released in this process might act as activation agents. On the other hand, the heat treatment of CM left the porosity unaltered. High-temperature doping of the CM surface with nitrogen or sulfur noticeably decreased the surface area, having a pronounced effect on the volume of very small micropores, especially in the case of nitrogen doping. This suggests that sulfur- and nitrogen-containing groups might be deposited at the entrances of these small pores and/or at the edges of distorted graphene layers where the most reactive surface sites are known to exist. Modification of the CMGO composite with hydrogen sulfide had a less pronounced effect on the decrease of surface area in comparison to that on CM. Interestingly, the decrease in the volume of ultramicropores for CMGO-S was more marked than that for CM-S (25% decrease in CMGO-S versus 20% for CM-S), which might be related to the reactivity of GO oxygen groups with hydrogen sulfide.

All of the changes described above are seen in a comprehensive way on the PSDs presented in Figure 3. The changes are mainly seen in the volume of ultramicropores with an average diameter of \sim 0.6 nm, which markedly decreased as a

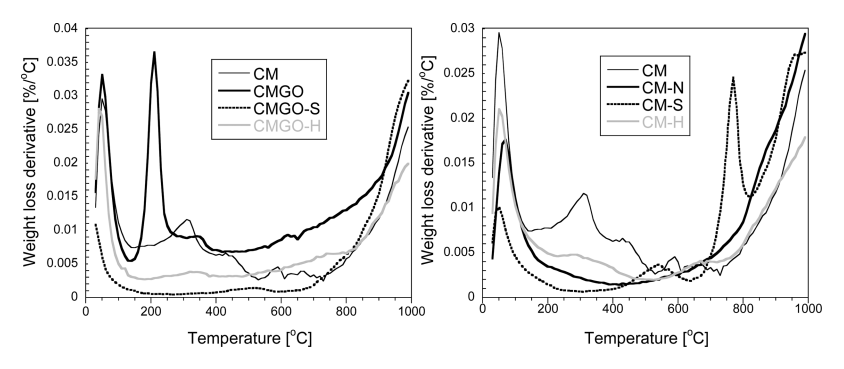


Figure 5. DTG curves in air for the samples tested.

Table 3. Results of Deconvolution of C 1s, O 1s, S 2p, and N 1s Core Energy Levels

energy, eV	bond assignment	СМ	СМ-Н	CMGO	CMGO-H	CM-N	CM-S	CMGO-S
O//	C	C 1s						
284.8	C-(C, S) (graphitic carbon)	73.0	66.9	62.7	78.7	77.9	80.1	78.9
286.3	C-(O, N, S, H) (phenolic, alcoholic, etheric)	14.9	19.4	17.5	12.1	13.1	12.5	12.4
287.1	C=O (carbonyl or quinone)	8.0	9.4	14.6	5.1	5.4	4.9	5.0
288.6	O-C=O (carboxyl or ester)	2.2	2.1	3.1	2.4	3.4.	1.7	2.1
290.0	π – π *	1.8	2.2	2.1	1.6	1.2	0.8	1.6
		O 1s						
531.5	O=C/O=S (in carbonyl/quinone or sulfoxides/sulfones)	7.3	5.2	9.7	9.0	5.6	8.9	3.2
533.0	O-C/O-S (in phenol/epoxy or thioethers/sulfonic)	82.6	80.9	71.9	85.7	90.9	71.9	86.1
534.35	-O- (in carboxyl, water or chemisorbed oxygen species)	10.1	13.9	18.3	5.3	3.4	18.3	10.6
		N 1s						
398.5	N-6 (in pyridine)		46.1		46.3	47.8		
400.5	N-5 (in pyrrolic/pyridone and azo nitrogen)		53.9		53.7	33.3		
402.4	N-X (in pyridine N-oxide)					18.9		
		$S\ 2p_{3/2}$						
164.0	R-S-S-, C-S-C (in bisulfides/thiophenes configurations)						83.0	100.
167.3	R_2 -S=O/R-SO ₂ -R (in sulfoxides, sulfones)						17.0	

result of the applied modifications. Nevertheless, the size of pores remained unchanged. The only exception is CMGO-S, for which the size of ultramicropores increased to 0.7 nm, and larger micropores with diameters between 0.8 and 0.9 nm seen in other carbons were not detected in this material. These changes might affect the ORR process on CMGO-S.³⁷

In addition to their effects on porosity, the modifications applied were expected to alter surface chemistry to an even greater extent. Potentiometric titration provides information about the average surface pH, number of acidic groups on the surface, and the distributions of their pK_a values. The proton binding curves are presented in Figure 4, and the number of strong and weak acidic groups and surface pH values are collected in Table 2. The details on the pK_a distributions are presented in Figure 2S and Table 1S in the Supporting Information. All samples exhibit basic pH and show a proton uptake indicating the basic character of their surfaces. The composite with GO is the least basic and exhibits a very small extent of the proton release process. This is due to the strongly acidic character of GO located inside the pores of this sample. The highest pH values and the smallest numbers of dissociating groups are on the surface of CM-H and on those of the sulfurmodified samples, CM-S and CMGO-S. Interestingly, the nitrogen-modified sample is very rich in groups dissociating in our experimental pH window.

To further investigate the differences in surface chemistry, TG analysis in helium was carried out and the differential (DTG) curves are collected in Figure 5. The TG curves are

included in Figure 3S in the Supporting Information. On DTG curves, the peaks represent the weight losses related to the decomposition of surface groups, and the areas under them are directly proportional to the weight loss/amount of decomposing groups. A peak at about 100 °C represents the desorption of physically adsorbed water. For CM, carboxylic groups decompose between 200 and 400 °C, followed by the decomposition of anhydrides and lactones at about 600 °C. 47,48 At temperatures higher than 700 °C, phenol, ether, and carbonyl structures decompose. On the other hand, the addition of GO results in the appearance of a sharp peak at 200 °C representing the decomposition of epoxy groups of GO. Its OH groups decompose at temperatures higher than 800 °C. Heating both CM and CMGO at 950 °C evidently "cleans" their surfaces from surface groups, which is consistent with the potentiometric titration results. While the nitrogen-doped sample shows gradual weight loss mainly between 100 and 400 °C and over 800 °C, sulfur-modified carbons show markedly different patterns. On the DTG curve for CMGO-S, a very small weight loss between 400 and 600 °C is revealed. This is followed by an increasing weight loss at temperatures higher than 700 °C. The DTG curve for CM-S, in addition to weight losses in the same range of temperature as those for the composite, reveals intense peaks at 700 and 800 °C. This indicates differences in sulfur chemistry between these two sulfur-doped samples. The composite is apparently chemically more homogeneous. The weight loss between 400 and 600 $^{\circ}\text{C}$ can be linked to the decomposition of sulfoxide/sulfone bonds

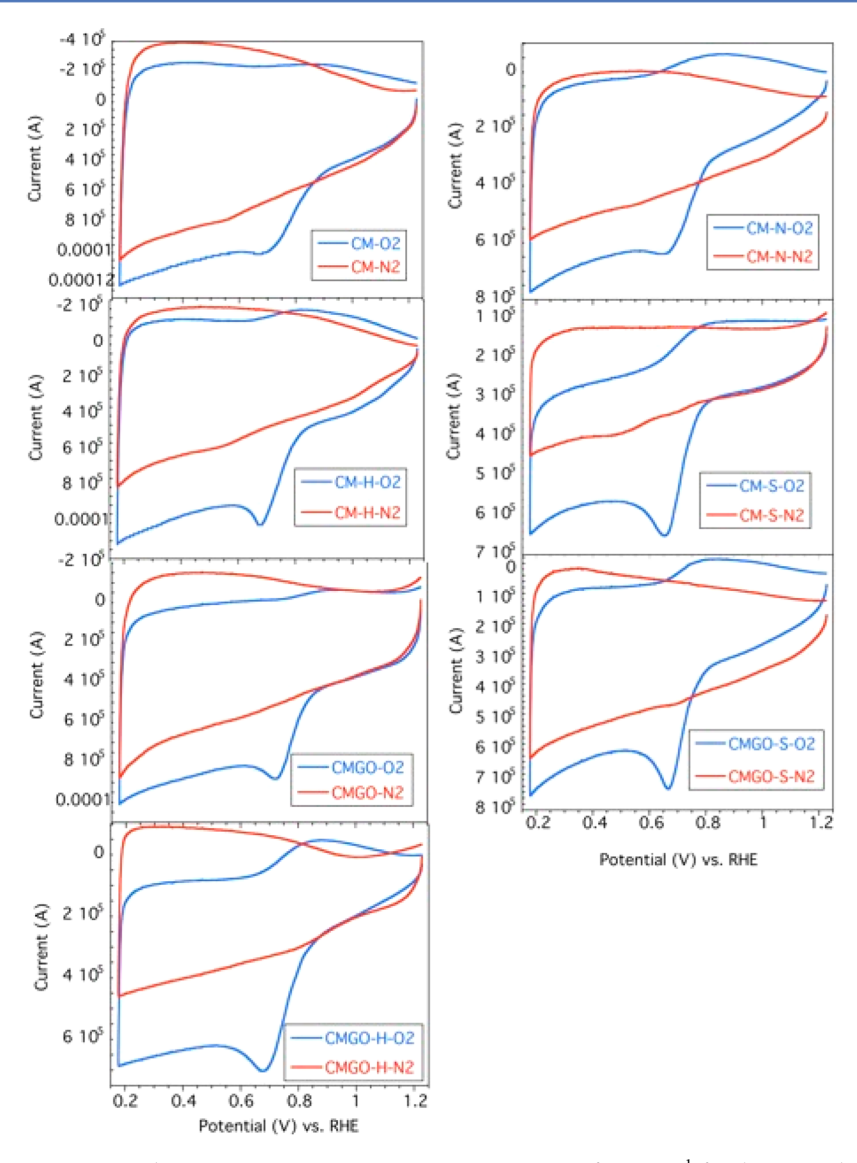


Figure 6. Cyclic voltammograms measured using RRDE in 0.10 M KOH at a scan rate of 5 mV s⁻¹ for the materials studied.

and that at temperatures higher than 750 °C to the decomposition of sulfur in sulfides and thiophenic configurations. ⁴⁹ Small intensities of the peaks representing losses of physically adsorbed water suggest the high hydrophobicity of the sulfur-doped samples.

The view of surface chemistry derived from the potentiometric (PT) and thermogravimetric (TG) analyses is supported by the XPS analysis. The atomic content of elements on the surface is presented in Table 2. Interestingly, nitrogen was detected not only on the surface of CM-N but also on the heattreated CM and CM-H. Its presence is related to the use of hexamine as cross-linker in the synthesis procedure. It forms complexes with tannin that are incorporated in the thermoset polymer structure, 40 and some of these nitrogenated moieties are the residue of this process. Lack of detected nitrogen on CM and CMGO can be linked to the screening effect of oxygen groups on the surface. Upon their decomposition and removal of carbon atoms as a result of heat treatment, as suggested by the TG and PT data, nitrogen groups are exposed and detected by XPS on these samples. On the surface of the H₂S-treated samples, nitrogen was also not detected, and on CM-S and CMGO-S only less than 1 and 1.2 atom % sulfur were found,

respectively. These two samples have also the smallest contents of oxygen. However, on CMGO-H, as expected, heat treatment decreased almost twice the content of oxygen mainly due to the reduction of GO, the content of oxygen on the surface of CM and CM-H being basically the same after such treatment. Even though this is consistent with the PT results, the TG analysis showed a marked difference in weight loss between these two samples. A plausible explanation is the difference in the principles of the methods. While both XPS and PT are surface techniques, TG is a bulk analysis, where the content of the carbon matrix is also included. A very high content of oxygen in CM-N is consistent with the potentiometric titration results.

More details on the surface chemistry are provided by the deconvolution of the C 1s, O 1s, N 1s, and S 2p core energy levels^{24,29} (see Table 3 and Figure 4S in the Supporting Information). Analysis of the contributions of C 1s did not show very large differences between the samples. The only noticeable difference was in the case of the contribution at 286.3 eV for CM-H in comparison to that for CM. This contribution, in addition to phenolic groups, can be related to the nitrogen in C−N bonds. The CMGO sample has the marked contributions of carbon in C−O and C≡O bonds

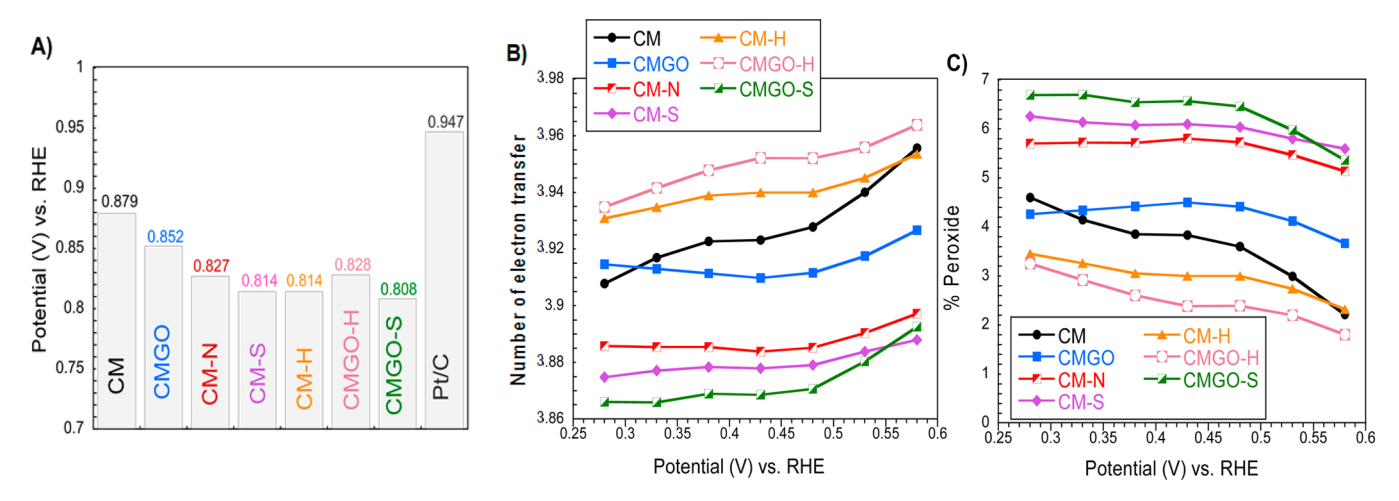


Figure 7. Comparison of the onset potential (A), number of electron transfer (B), and the percentage of oxygen reduced to peroxide (C).

related to the presence of GO. These groups were reduced after heat treatment, and the contribution of C–C bonds in sp² configuration significantly increased. Sulfur-doped samples and CMGO-H have the smallest contributions at high binding energies on C1s spectra, indicating the lowest level of oxidation. This is consistent with a low content of oxygen on their surfaces and with the smallest amounts of acidic groups detected using potentiometric titration.

The deconvolution of O 1s core energy level spectra showed three contributions for all samples: oxygen in carbonyl/ quinones and sulfoxides/sulfones at 531.3 eV, phenol, epoxy, and thioester/sulfonic groups at 533 eV, and carboxyl, water, or chemisorbed oxygen species at 543.3 eV. The contribution at 531.3 eV was the smallest for CNGO-S but the highest for CMGO. On the other hand, the latter sample had the smallest contribution at 533 eV (phenol, epoxy) but the highest contribution of carboxylic acid/chemisorbed oxygen. Heating at 950 °C significantly decreased that contribution. No significant change was found for the distribution of oxygen species for CM-H. Interestingly, for CM-N the contribution of oxygen in phenol and epoxy groups is the highest. For this sample, and although the signal is noisy owing to the low sensitivity of the instrument used, the deconvolution of N 1s indicates the presence of species at a binding energy of 402.4 eV linked to pyridinic N-oxide. This can explain the high content of oxygen in this sample. On the surface of CM-H and CMGO-H, nitrogen is present only as pyridine and pyrrolic/azo nitrogen. As indicated above, this nitrogen originates from the nature of the cross-linker (hexamine, C₆H₁₂N₄) used to prepare the carbon foams.

The deconvolution of S 2p core energy levels shows that in CMGO-H sulfur is present only in a reduced form as bisulfide and thiophenes, and in CN-S there is a small contribution of sulfoxides at 167.3 eV. This chemical heterogeneity was also seen in the TG curves and was discussed above (Figure 5).

To ensure that the materials tested do not contain transition metals such as iron, known as an ORR catalyst, the ash composition of the parent CM sample was analyzed. The detailed results are presented in Table 2S in the Supporting Information. The main components of ash are K, Mg, and Ca, whose contents in the original sample are 8196, 3044, and 2757 ppm. The content of iron is only 1 ppm, and it is 4 orders of magnitude smaller than that in the work of Dai and co-workers, who found 1.1 wt % in their carbon-based purified catalyst.³⁹

On a purified sample with only 0.11% of iron, the ORR activity significantly decreased. Therefore, no marked catalytic effect on the catalytic performance of our carbons is to be expected.

The water uptake is directly linked to surface chemistry affecting the polarity/hydrophilicity level (Table 1). Even though the porosity can play some role, generally it is accepted that the less water adsorbed, the more hydrophobic the surface. Heating at 950 °C decreases the affinity of the surface toward water owing to the decomposition of oxygen-containing groups. The most hydrophobic foams are CM-H and CM-S. CMGO-H and CMGO-S have similar levels of hydrophobicity. Some affinity of the latter sample to adsorb water can be related to its higher volume of mesopores. In fact, functional groups containing oxygen can only exist in pores larger than 1 nm (supermicropores and mesopores) and they are mainly responsible for attracting water. They are also expected to attract an aqueous electrolyte with dissolved oxygen; however, on the basis of their volume, the highest amount of oxygen is expected to be adsorbed in the pores of CM and CMGO-H and the smallest amount in CM-N and CMGO-S, provided that the electrolyte has the same access to the entrance of the pores smaller than 0.7 nm. Obviously, the situation is more complex and surface chemistry is expected to affect that access. The distribution of catalytic centers is also expected to play an important role.

3.2. Electrochemical Performance in Alkaline Solution. The cyclic voltammogram (CV) curves measured in 0.1 M KOH electrolyte saturated with either O₂ or N₂ are presented in Figure 6. In each case the geometrical surface of the electrode was kept the same. The CV curves for Pt/C were reported previously.³⁷ The maximum of the ORR hump for this sample is at 0.85 V vs RHE. The most pronounced humps related to oxygen reduction are seen for CM-S, GM-H, and CMGO-H. These samples also happened to be the most hydrophobic, as shown in Table 1. Even though a smaller amount of water was adsorbed on CM-N than on CMGO-H, this trend can be linked to the almost twice smaller surface area of the former sample.

The onset potentials, defined as the highest potentials at which the ORR reaction starts, are compared in Figure 7A. The comparative plot of the LSV results at a rotation speed of 2000 rpm is presented in Figure 7S in the Supporting Information. The CM sample exhibited the most positive onset potential. Addition of GO made it less positive. Heating both CM and

CMGO at 950 °C also made the onset potential less positive. Interestingly, the extent of that decrease effect on the onset potential for CMGO-H is much smaller than that for CM-H. As was proposed previously,³⁷ the observed effect of these modifications on the onset potential can be directly linked to some changes in the porosity and in the degree of hydrophilicity. Obviously, the addition of GO resulted in a much more hydrophilic surface in comparison to that of CM. The porosity in the range of small pores decreased, and this resulted in less affinity of the surface to withdraw oxygen from electrolyte for its adsorption in small pores, promoting the reduction reaction. Heating CMGO at 950 °C markedly decreased its oxygen content and also made the surface much more hydrophobic as seen from the deconvolution of C 1s and O 1s. Its porosity became comparable to that of CM. Nevertheless, water showed more affinity to adsorb on CMGO-H than on CM, which is also seen in the higher number of groups dissociating in our pH window (Table 2 and Table 1S in the Supporting Information). This results in the less positive onset potential on CMGO-H in comparison to that on CM. The heat treatment of CM, interestingly, introduced an increased contribution of carboxylic groups (from O 1s deconvolution) and decreased the volume of pores smaller than 0.7 nm, and these changes had a negative effect on the onset potential.

In the case of heteroatom-doped samples, in addition to the effects of hydrophobicity and porosity, the catalytic influence of nitrogen- and sulfur-containing groups is of paramount importance. Among these samples, that treated with nitrogen showed the most positive onset potential and the behaviors of the two S-containing samples were very similar to the slightly better performance of CM-S. All of these samples have a lower volume of narrow pores (<0.7 nm) in comparison to CM and the CMGO series. In fact, CM-N shows the smallest volume of these pores, which are effective in promoting the adsorption of oxygen. Interestingly, this sample has the highest content of oxygen and groups dissociating in our pH window. This suggests that the reduction of oxygen must be predominantly the effect of catalytic sites associated with nitrogen 10 and not that of porosity. Even though the catalytic effect related to sulfur sites should also dominate the oxygen reduction on CM-S and CMGO-S, the higher hydrophobicity, the lower oxygen content, and the higher surface area of the CM-S surface might slightly enhance its performance in comparison to that of CMGO-S, owing to the contribution of the pore effect to the oxygen reduction mechanism in this case. Recent studies on the positive effects of porosity on ORR activity indicate that a high volume of pores is important for the high dispersion of metalfree catalytic centers that enhance ORR. 33,36,5

The oxygen reduction can occur via four-electron pathways where O₂ is directly reduced to water, or two-electron pathways where O₂ is reduced to peroxide and consequently to water. The two-electron process is detrimental in fuel cells, as the peroxide leads to corrosion of the cell components, eventually leading to a decrease in the fuel cell efficiency. From the results collected, the number of electron transfer and the percent peroxide were calculated and are presented in Figure 7B,C, respectively. As expected, there is a reverse relationship between the amount of hydrogen peroxide detected and the number of electron transfer with respect to the potential (Figure 7C). Even though the number of electron transfer for all samples tested is close to 4, small differences exist. Thus, CMGO-H has the highest number of electron transfer between

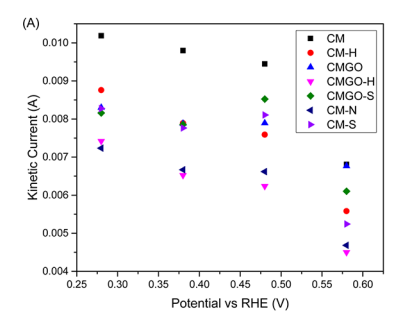
3.96 and 3.93 in the potential range of 0.58–0.28 V (vs RHE) and the smallest peroxide yield (1.81–3.25%), indicating a predominant reduction of oxygen to water. The order in decreasing n value is as follows: CMGO-H > CM-H > CM > CMGO > CM-N > CM-S = CMGO-S. The opposite trend was found in hydrogen peroxide concentration. The highest numbers of electron transfer were found for the series of CM and CM-GO and the smallest for the heteroatom-doped samples, which might be related to the differences in the mechanism indicated above. Nevertheless, for the onset potential, the CM-N sample outperformed those doped with sulfur. On the latter, once again no marked differences in the n value were found.

To study the influence of the electron transfer kinetics on ORR on the vitreous carbon foams, RRDE experiments were conducted in 0.1 M KOH solution at different rotation speeds from 400 to 2000 rpm (Figures 5S and 6S in the Supporting Information). The current density increased with an increased rotation speed due to the enhanced diffusion of the electrolytes and O_2 . A Koutecky–Levich (K-L) plot was used to analyze kinetic parameters such as kinetic current density (J_k) and the effective diffusion coefficient of O_2 (D_0). The equation to calculate the K-L plot is 43

$$1/J = 1/J_1 + 1/J_k = 1/(B\omega^{0.5}) + 1/J_k \tag{5}$$

where J is the measured current density, J_1 and J_k are the diffusion-limiting and kinetic-limiting current densities, ω is the rotation rate of the electrode, and B is the Levich constant. B can be calculated using the equation $B=0.62nFC_0(D_0)^{2/3}\nu^{-1/6}$ and $Jk=nFkC_0$, where n is the number of electron transfer in the ORR, F is the Faraday constant (F=96485 C mol $^{-1}$), D_0 is the effective diffusion coefficient of O_2 (cm 2 s $^{-1}$), ν is the kinematic viscosity of the electrolyte (cm 2 s $^{-1}$), C_0 is the oxygen concentration (mol cm $^{-3}$), and k is the electron transfer rate constant. The K-L plot for the as-prepared samples at an electrode potential of 0.58 V (vs RHE) exhibited linearity at the low rotation speed regime (Figure 7S in the Supporting Information) where the linear fitting was performed. 51,52

The slope and intercept of the linear part of the K-L plot give the Levich constant (B) and J_k , which are used to calculate the effective diffusion coefficient constant of $O_2(D_0)$ (Figure 7S in the Supporting Information) and the kinetic rate constant k. The doped samples CM-N, CMGO-S, and CM-S have the highest kinetic rate constant, indicating the intrinsic good performance of the heteroatom-doped samples. For the nonheteroatom-doped samples, the kinetic rate constant and the effective diffusion coefficient exhibit the same trend as the $V_{\rm mic}$ / V_t ratio, suggesting that when catalytic dopants are not present, the micropore volume advances the oxygen diffusion and the reduction reaction. In fact, CM also has the highest surface area. The order in the accessibility of the pores to oxygen is as follows: CM > CM-H > CMGO > CMGO-H for the nondoped samples and CM-N > CMGO-S > CM-S for the doped samples. That order more or less follows the order of the surface area, and some discrepancies are, for instance, that the diffusion of oxygen on CM-N is better than that in CM-S, even though the surface area of the latter is markedly higher. This suggests that the diffusion of oxygen is influenced by the number of oxygen groups. More oxygen on the surface of CM-N promotes a higher degree of wettability of the pore system and thus the electrolyte with dissolved oxygen can get closer to the hydrophobic pores/catalytic centers.



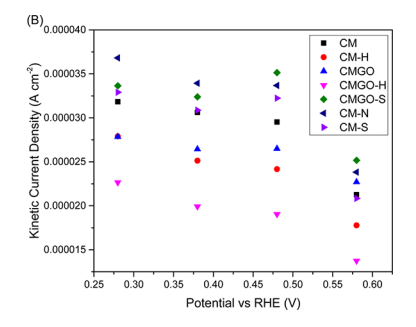


Figure 8. Kinetic current (A) and kinetic current density (B).

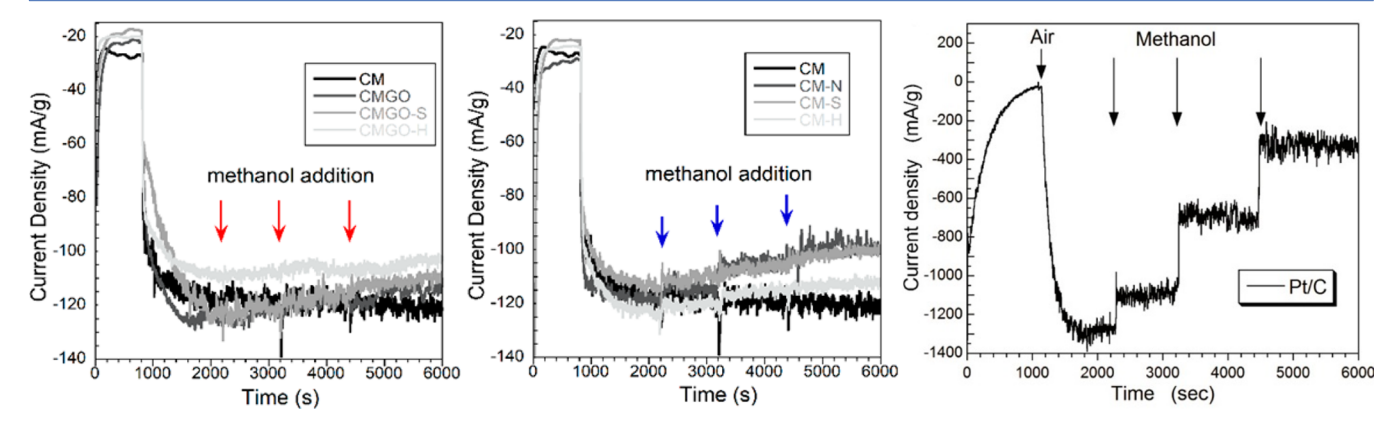


Figure 9. Chronoamperometry response for methanol crossover at the potential of the maximum of the oxygen reduction humps. Results of methanol crossover tests on Pt/C are reprinted with permission from ref 37. Copyright 2016, American Chemical Society.

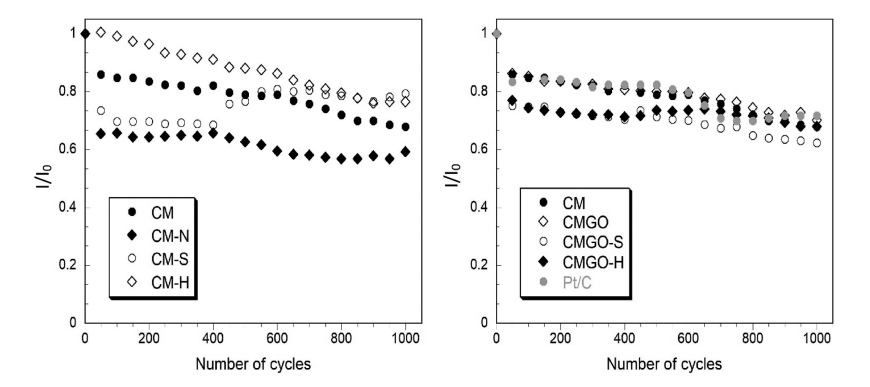


Figure 10. Stability of CM, CM-N, CM-S, CM-H, CMGO, CMGO-S, CMGO-H, and Pt/C in the ORR process over 1000 CV cycles.

The kinetic currents are compared in Figure 8A. In terms of absolute value of the kinetic current, CM outperformed heteroatom-modified carbon foams. Although the kinetic rate constant for CM is not as high as those of the heteroatom-doped samples, the outstanding overall performance of CM can be rationalized by combining its high surface area and high $V_{\rm mic}/V_{\rm t}$ ratio. The surface area of CM is 1.6 times that of CM-N and $V_{\rm mic}$ of CM is 1.64 times that of CM-N. The kinetic current of CM is around 1.44 times that of CM-N, which obeys the similar ratio of $V_{\rm mic}$ indicating the close relationship between the micropores and the performance toward ORR.

Since in our discussion we stressed the role of small pores combined with hydrophobicity in the process of oxygen reduction, the current densities calculated from the surface area on the basis of BET measurements are compared in Figure 8B. However, for the CM and CM-GO series, the heteroatom-doped samples presented a totally different picture of the catalytic activity. Now CM-N is the best-performing sample,

and the performance of the sulfur-doped carbons is similar to that of CM. This confirms the different mechanism and the effects of the catalytic center of these samples on the ORR. Interestingly, some nitrogen was detected on the surface of CM-H and CMGO-H (Table 3) but that nitrogen seems not to affect the ORR to the same extent as that on CM-N. In fact, in the literature a quaternary nitrogen, not detected on the surface of our materials, was indicated as enhancing the ORR. ¹⁰ The only difference between the nitrogen-containing samples is that CM-N has nitrogen in pyridine *N*-oxides. They have a positive charge on nitrogen, and the results suggest that these species can have a catalytic effect on the ORR.

All carbons tested show a very high tolerance to methanol crossover at the potential of the maximum current of ORR (Figure 9). Indeed, injecting 0.2 mL of methanol three subsequent times (indicated as arrows in Figure 9) did not affect the current density in the case of the catalysts tested. On the other hand, when Pt/C was tested under the same

conditions, a significant decrease in the current was noticed for each addition of methanol to the electrolyte, indicating a decrease in the activity of catalytic Pt-based centers.

Stability tests were run arbitrarily to 1000 potential cycles (Figure 10). The best stability, better than that of Pt/C, was found for CM-H, whose performance after 1000 cycles remained at the 80% level. The stability of Pt/C decreased to about 70%, and it is very similar to that of the parent CM sample and CMGO. Interestingly for CM-S after the initial 30% decrease in the performance in 400 cycles, the current density gradually increased and reached a plateau at the same level as for CM-H. This might be related to the instability of sulfur compounds in this sample, which are likely oxidized by H2O2 formed in situ. The worst performance from the point of view of stability is presented by heteroatom-doped CM-N and CMGO-S. The current significantly drops at the beginning of the cycling tests, and after 1000 cycles it remains at about 60% of the initial performance. One of the factors affecting the stability is the speciation of the oxygen reduction products. If a marked quantity of H₂O₂ is formed (Figure 7), the oxidation of the carbon surface is expected. Indeed, the highest amounts of hydrogen peroxide were formed in the cases of GMGO-S, CM-S, and CM-N. Thus, oxidation of the surface resulting in either removal/change of active centers or changes in the porosity can be responsible for the loss of catalytic performance. As expected, the effect is the strongest on the first exposure to oxidizing agent. An increase in the activity of CM-S after a certain number of cycles is likely caused by oxidation and removal of sulfur species, which might result in a surface similar to that of CM-H. These two samples were treated at 950 °C in either nitrogen or hydrogen sulfide.

Even though an analysis of the results collected indicates the marked role of small pores with a hydrophobic surface as catalytic sites for ORR, which advance the reduction by a mechanism different from that on heteroatom-containing sites, these findings are not contradictory to those published in the literature indicating the role of defects in the carbon matrix in ORR reduction. In fact, a more developed surface obviously leads to more defects in the carbon matrix, which were indicated by Hu and co-workers and Dai and co-workers as the ORR reduction sites. Moreover, our modification with GO was in line with findings by Dai and co-workers. They suggested that graphene oxide fragments formed by oxidation of their CNTs increased the ORR activity, and in our case, the addition of GO to CM indeed increased the performance in terms of onset potentials. The treatment of CMGO at 950 °C might create more active defects enhancing the catalytic activity and the number of electron transfer.

Further support for our findings on the specific and important role of porosity is the recent results published on 3D interconnected carbon networks. ^{50,53–55} Even though some of those structures contained nitrogen and Fe or Co, the interconnecting network architectures were indicated as promoting the ORR by facilitating electron transfer and providing a high dispersion of active sites.

4. CONCLUSIONS

The results presented in this paper emphasize the role of small pores and their surface hydrophobicity in ORR on carbonaceous materials. We proposed and explored a new mechanism of O_2 reduction which is based on a principle different from the generally accepted mechanism of ORR reduction on heteroatom-doped carbons. Even though some carbon foams

investigated here do not have "classical" catalytic centers for ORR, on the basis of nitrogen and sulfur incorporated to the carbon matrix, they show a promising onset potential, a number of electron transfer close to 4, and a relatively good kinetic current density. Such performance is linked to the specific porosity where small micropores and mesopores coexist. The macropores promote the wettability of the surface with electrolyte, whereas micropores present in thick foam walls are the sites where oxygen reduction takes place. Owing to the hydrophobicity of the ultramicropores (smaller than 0.7 nm), water does not have a tendency to enter them. At their entrances, oxygen, which adsorbs on hydrophobic surfaces, moves from the aqueous phase to these pores, where it is strongly adsorbed owing to the overlapping adsorption potential. Then the reduction process takes place and oxygen is reduced mainly to water. The formed water does not stay in hydrophobic pores but rather is strongly attracted to larger pores. When this happens, the pore-oxygen reduction sites can efficiently adsorb/withdraw other O2 molecules from the electrolyte. For this process the number of small pores is important. Even though we are not aware of the methods which could be used to calculate the number of pores in amorphous carbons, the differences in the volume of pores smaller than 0.7 nm between samples can be considered as an indication of such pore number. Even though the hydrophobicity in these pores and their sizes are crucial, some level of polarity in larger pores is beneficial to transport oxygen dissolved in the electrolyte to the entrances of these small pores.

On the other hand, the modification of the carbon surface with heteroatoms applied in this work decreased the porosity as well as introduced the heteroatom dopant-based catalytic centers promoting the ORR. This dramatically changed the mechanism of the ORR. Still, the number of electron transfer was close to 4 but with a less positive onset potential. We also noticed that, even though the current density can be increased due to the introduction of more active centers, catalytic centers from these heteroatom dopants are nevertheless not stable upon generation of oxidative species, such as H_2O_2 during the ORR process.

The results obtained suggest that nondoped carbons can be used as efficient ORR catalysts. Such materials can be a more cost effective alternative to Pt/C than heteroatom-doped graphene. Tuning the porosity and surface chemistry of porous carbons is crucial to fully use the promise that the small pores provide for the ORR. This new mechanism we propose is based on the affinity of oxygen to strongly adsorb in small hydrophobic pores. The results presented offer an alternative/complementary route to explain the ORR activity of porous carbon-based catalysts addressed recently in the literature.

ASSOCIATED CONTENT

S Supporting Information

The Supporting Information is available free of charge on the ACS Publications website at DOI: 10.1021/acscatal.7b01977.

Nitrogen adsorption isotherms, TG curves, pK_a distributions, deconvolutions of core energy level spectra, linear sweep voltammograms, K-L plots, and results of ICP analysis (PDF)

AUTHOR INFORMATION

Corresponding Author

* E-mail: tbandosz@ccny.cuny.edu.

ORCID

Teresa J. Bandosz: 0000-0003-2673-3782

Notes

The authors declare no competing financial interest.

ACKNOWLEDGMENTS

The French group gratefully acknowledges the financial support of the CPER 2007-2013 "Structuring the Competitiveness Fibre Cluster", through local (Conseil Général des Vosges), regional (Région Lorraine), national (DRRT and FNADT,) and European (FEDER) funds. The HE group acknowledges the financial support provided by the National Science Foundation (CBET 1438493 and DMR 1507812). The authors are grateful to Dr. Mykola Seredych for his experimental involvement in sample modifications and in collecting some surface characterization data and to Dr. Dimitrios Giannakoudakis for collecting SEM images of a high magnification. Mr. Albert V. Tamashausky from Asbury Carbons is thanked for providing ICP analysis data.

REFERENCES

- (1) Steele, B. C. H.; Heinzel, A. Nature 2001, 414, 345-352.
- (2) Armand, M.; Tarascon, J. M. Nature 2008, 451, 652-657.
- (3) Liu, M.; Zhang, R.; Chen, W. Chem. Rev. 2014, 114, 5117-5160.
- (4) Li, Y.; Zhou, W.; Wang, H.; Xie, L.; Liang, Y.; Wei, F.; Idrobo, J. C.; Pennycook, S. J.; Dai, H. Nat. Nanotechnol. **2012**, *7*, 394–400.
- (5) Gong, K. P.; Du, F.; Xia, Z. H.; Durstock, M.; Dai, L. M. Science **2009**, 323, 760–764.
- (6) Yang, S.; Zhi, L.; Tang, K.; Feng, X.; Maier, J.; Mullen, K. Adv. Funct. Mater. 2012, 22, 3634–3640.
- (7) Yang, Z.; Yao, Z.; Li, G.; Fang, G.; Nie, H.; Liu, Z.; Zhou, X.; Chen, X.; Huang, S. ACS Nano 2012, 6, 205-211.
- (8) Zhang, C.; Hao, R.; Lian, H.; Hou, Y. Nano Energy 2013, 2, 88-97.
- (9) Liang, J.; Jiao, Y.; Jaroniec, M.; Qiao, S. Z. Angew. Chem. 2012, 124, 11664–11668; Angew. Chem., Int. Ed. 2012, 51, 11496–11500.
- (10) Liang, J.; Zheng, Y.; Chen, J.; Liu, J.; Hulicova-Jurcakova, D.; Jaroniec, M.; Qiao, S. Z. Angew. Chem. **2012**, 124, 3958–3962; Angew. Chem., Int. Ed. **2012**, 51, 3892–3896.
- (11) Seredych, M.; Bandosz, T. J. Carbon 2014, 66, 227-233.
- (12) Wang, L.; Ambrosi, A.; Pumera, M. Angew. Chem. 2013, 125, 14063–14066; Angew. Chem., Int. Ed. 2013, 52, 13818–13821.
- (13) Silva, R.; Voiry, D.; Chhowalla, M.; Asefa, T. J. Am. Chem. Soc. **2013**, 135, 7823–7826.
- (14) Tao, G.; Zhang, L.; Chen, L.; Cui, X.; Hua, Z.; Wang, M.; Wang, J.; Chen, Y.; Shi, J. Carbon 2015, 86, 108–117.
- (15) Chen, J.; Zhang, H.; Liu, P.; Li, Y.; Li, G.; An, T.; Zhao, H. Carbon 2015, 92, 339–347.
- (16) Zhang, J.; Dai, L. ACS Catal. 2015, 5, 7244-7253.
- (17) Daems, N.; Sheng, X.; Vankelecom, I. F. J.; Pescarmona, P. P. J. Mater. Chem. A **2014**, 2, 4085–4110.
- (18) Wu, J.; Yang, Z.; Li, X.; Sun, Q.; Jin, C.; Strasser, P.; Yang, R. J. Mater. Chem. A **2013**, 1, 9889–9896.
- (19) Wu, G.; More, K. L.; Johnston, C. M.; Zelenay, P. Science 2011, 332, 443-447.
- (20) Watson, V. J.; Delgado, C. N.; Logan, B. E. Environ. Sci. Technol. **2013**, 47, 6704–6710.
- (21) Choi, C. H.; Park, S. H.; Woo, S. ACS Nano 2012, 6, 7084–7091.
- (22) von Deak, D.; Biddinger, E. J.; Luthman, K.; Ozkan, U. S. Carbon 2010, 48, 3637–3639.

- (23) Zhong, M.; Kim, E. K.; McGann, J. P.; Chun, S. E.; Whitacre, J. F.; Jaroniec, M.; Matyjaszewski, K.; Kowalewski, T. *J. Am. Chem. Soc.* **2012**, *134*, 14846–14857.
- (24) Seredych, M.; László, K.; Rodríguez-Castellón, E.; Bandosz, T. J. Energy Chem. 2016, 25, 236–245.
- (25) Seredych, M.; László, K.; Bandosz, T. J. ChemCatChem 2015, 7, 2924–2931.
- (26) Wang, S.; Zhang, L.; Xia, Z.; Roy, A.; Chang, D. W.; Baek, J.-B.; Dai, L. Angew. Chem., Int. Ed. **2012**, *51*, 4209–4212.
- (27) Li, H.; Kang, W.; Wang, L.; Yue, Q.; Xu, S.; Wang, H.; Liu, J. Carbon 2013, 54, 249–257.
- (28) Seredych, M.; Biggs, M.; Bandosz, T. J. Microporous Mesoporous Mater. **2016**, 221, 137–149.
- (29) Seredych, M.; Rodriguez-Castellon, E.; Bandosz, T. J. J. Mater. Chem. A 2014, 2, 20164–20176.
- (30) Wiggins-Camacho, J. D.; Stevenson, K. J. J. Phys. Chem. C 2011, 115, 20002–20010.
- (31) Yu, D.; Nagelli, E.; Du, F.; Dai, L. J. Phys. Chem. Lett. 2010, 1, 2165-2173.
- (32) Dai, L.; Xue, Y.; Qu, L.; Choi, H. J.; Baek, J. B. Chem. Rev. 2015, 115, 4823-4892.
- (33) Kim, M.; Kim, H. S.; Yoo, S. J.; Yoo, W. C.; Sung, Y.-E. *J. Mater. Chem. A* **2017**, 5, 4199–4206.
- (34) Wang, L.; Tang, Z.; Yan, W.; Yang, H.; Wang, Q.; Chen, S. ACS Appl. Mater. Interfaces 2016, 8, 20635–20641.
- (35) Park, Y.-C.; Tkiwa, H.; Kakinuma, K.; Watanabe, M.; Uchida, M. J. Power Sources **2016**, 315, 179–191.
- (36) Yin, X.; Lin, L.; Chung, H. T.; Komini Babu, S.; Martinez, U.; Purdy, G. M.; Zelenay, P. Presented at 231st ECS Meeting, New Orleans, May 28–June 1, 2017.
- (37) Seredych, M.; Szczurek, A.; Fierro, V.; Celzard, A.; Bandosz, T. J. ACS Catal. **2016**, *6*, 5618–5628.
- (38) Jiang, Y.; Yang, L.; Sun, T.; Zhao, J.; Lyu, Z.; Zhuo, O.; Wang, X.; Wu, Q.; Ma, J.; Hu, Z. ACS Catal. **2015**, 5, 6707–6712.
- (39) Li, Y.; Zhou, W.; Wang, H.; Xie, L.; Liang, Y.; Wei, F.; Idrobo, J.-C.; Pennycook, S. J.; Dai, H. Nat. Nanotechnol. **2012**, *7*, 394–400.
- (40) Szczurek, A.; Fierro, V.; Pizzi, A.; Stauber, M.; Celzard, A. Carbon 2013, 65, 214-227.
- (41) Szczurek, A.; Fierro, V.; Pizzi, A.; Celzard, A. Carbon 2013, 58, 245-8.
- (42) Hummers, W. S.; Offeman, R. E. J. Am. Chem. Soc. 1958, 80, 1339.
- (43) Ferrero, G. A.; Preuss, K.; Fuertes, A. B.; Sevilla, M.; Titirici, M. M. J. Mater. Chem. A 2016, 4, 2581–2589.
- (44) Jagiello, J.; Olivier, J. P. Adsorption 2013, 19, 777-783.
- (45) Jagiello, J.; Bandosz, T. J.; Schwarz, J. A. Carbon 1994, 32, 1026-1028.
- (46) Jagiello, J. Langmuir 1994, 10, 2778-2785.
- (47) Figueiredo, J.; Pereira, M. F.; Freitas, M. M.; Órfão, J. J. Carbon 1999, 37, 1379-1389.
- (48) Bandosz, T. J.; Ania, C. O. Surface chemistry of activated carbon and its characterization. In *Activated carbon surfaces in environmental remediation*; Bandosz, T. J., Ed.; Elsevier: Oxford, U.K., 2006; pp 159–230
- (49) Feng, W. G.; Kwon, S.; Feng, X.; Borguet, E.; Vidic, R. D. J. Environ. Eng. **2006**, 132, 292–300.
- (50) Baik, S.; Lee, J. W. RSC Adv. 2015, 5, 24661–24669.
- (51) Qu, L.; Liu, Y.; Baek, J.-B.; Dai, L. ACS Nano 2010, 4, 1321–1326.
- (52) Zurilla, R.; Sen, R.; Yeager, E. J. Electrochem. Soc. 1978, 125, 1103-1109.
- (53) Guo, Z.; Xiao, Z.; Ren, G.; Xiao, G.; Zhu, Y.; Dai, L.; Jiang, L. *Nano Res.* **2016**, *9*, 1244–1255.
- (54) Shi, Q.; Wang, Y.; Wang, Z.; Lei, Y.; Wang, B.; Wu, N.; Han, C.; Xie, S.; Gou, Y. *Nano Res.* **2016**, *9*, 317–328.
- (55) Fu, Y.; Tian, C.; Liu, F.; Wang, L.; Yan, H.; Yang, B. Nano Res. **2016**, *9*, 3364–3376.